Study on Seepage for Random Packed Porous Media Using the Lattice Boltzmann Method

jinfeng zhang[1], Zhongyue Li[1], Guangwei Liu[1], and Qinghe Zhang[2]

[1]Tianjin University
[2]State Key Laboratory of Hydraulic Engineering Simulation and Safety, Tianjin University

October 26, 2023

Abstract

The permeability coefficient of seepage is an important factor that is widely used in various engineering fields. There are numerous issues that influence the permeability coefficient, among which the porosity, particle size, particle size distribution and Reynolds number are of great importance. In this paper, a C++ code based on the three-dimensional lattice Boltzmann method (LBM) was developed and used to investigate the effects of the abovementioned factors on the permeability coefficient. A multiple relaxation time (MRT) collision scheme of the LB equations was used in the simulation. Porous media were prepared using the random packing method. Laminar flow and turbulent flow were simulated separately for particle Reynolds numbers in a range from 0.001 to 3,000. It was proven that in addition to the influence of porosity and particle size distribution on the permeability, the influence of the Reynolds number was obvious and could not be ignored. As the Reynolds number increased, the permeability of porous media decreased gradually. Based on the numerical simulation results, a modified formula for the permeability coefficient is proposed.

Hosted file

`976760_0_art_file_11511794_s2v474.docx` available at https://authorea.com/users/677426/articles/674561-study-on-seepage-for-random-packed-porous-media-using-the-lattice-boltzmann-method

Study on Seepage for Random Packed Porous Media Using the Lattice Boltzmann Method

Jinfeng Zhang[1,2], Zhongyue Li[1], Guangwei Liu[1*], and Qinghe Zhang[1]

[1]State Key Laboratory of Hydraulic Engineering Simulation and Safety, Tianjin University, Tianjin, 300072, China

[2]Key Laboratory of Earthquake Engineering Simulation and Seismic Resilience of China Earthquake Administration, Tianjin University, Tianjin, 300350, China

Corresponding author: Guangwei Liu (guangweiliu@tju.edu.cn)

Key Points:

- DNS to study the permeability coefficient for the laminar and turbulent seepage flow.
- The porosity, particle size, particle size distribution and Reynold number can affect the permeability coefficient.
- A modified formulation for the permeability coefficient is significant for porous medium seepage.

21   **Abstract**

22   The permeability coefficient of seepage is an important factor that is widely used

23   in various engineering fields. There are numerous issues that influence the

24   permeability coefficient, among which the porosity, particle size, particle size

25   distribution and Reynolds number are of great importance. In this paper, a C++ code

26   based on the three-dimensional lattice Boltzmann method (LBM) was developed and

27   used to investigate the effects of the abovementioned factors on the permeability

28   coefficient. A multiple relaxation time (MRT) collision scheme of the LB equations

29   was used in the simulation. Porous media were prepared using the random packing

30   method. Laminar flow and turbulent flow were simulated separately for particle

31   Reynolds numbers in a range from 0.001 to 3,000. It was proven that in addition to

32   the influence of porosity and particle size distribution on the permeability, the

33   influence of the Reynolds number was obvious and could not be ignored. As the

34   Reynolds number increased, the permeability of porous media decreased gradually.

35   Based on the numerical simulation results, a modified formula for the permeability

36   coefficient is proposed.

37

38   **1. Introduction**

39   Seepage phenomena play important roles in permeable seabeds and breakwaters.

40   The seepage of water through a sandy seabed beneath a breakwater is an important

41   consideration for its design and stability. However, the permeability of seepage is

42   difficult to predict because of the complexity of pore geometric characteristics and

43   pore connectivity.

44   Many scholars have conducted research on permeability through analytical

45   studies, experiments, field observations and numerical simulations. For example, an

46   experiment can be a simple way to calculate permeability by measuring the pressure

47   gradient and the flow rate (Despois and Mortensen, 2005; Rodríguez et al., 2004). For

48   saturated flow at a low Reynolds number, the mean flow rate of a viscous fluid

49   through a porous medium is inversely proportional to the viscosity and proportional to

50   the applied pressure difference. Darcy's law can be written as

51
$$-\frac{dP}{dx} = \frac{1}{K} \cdot (\mu \cdot V) \tag{1}$$

52   where $\frac{dP}{dx}$ is the pressure gradient, K is the permeability coefficient, μ is the

53   dynamic viscosity coefficient of the fluid, and V is the overall mean value of the

54   velocity in the x direction. The dimension of relative permeability K is length squared.

55   However, as velocities quicken, discrepancies between experimental data and

56   results obtained from Darcy's law appear. A term representing kinetic energy is

57   suggested to be added to Eq. 1:

58
$$-\frac{dP}{dx} = \frac{1}{K} \cdot (\mu \cdot V) + \beta \cdot (\rho \cdot V^2) \tag{2}$$

59   where β is the Forchheimer coefficient (also known as the non-Darcy coefficient) and

60   ρ is the density of the fluid.

61   The determination of parameters is very important. The available literature

62   provides many general formulas to calculate permeability and Forchheimer

63   coefficients based on porous media parameters such as porosity or tortuosity, but the

64   formulas are usually empirical and not universal (Sobieski and Trykozko, 2014).

65   Different formulas computed with a fixed set of parameters can lead to totally

66   different β coefficient values, ranging over several orders of magnitude.

67   Based on experimental data and theoretical analysis, the classic Kozeny–Carman

68   (KC) equation (Carman, 1997, 1939) that relates the permeability K to porosity ε has

69   been proposed:

70
$$K = \frac{\varepsilon^3}{C_{KC}\Gamma^2 S^2}$$
(3)

71   where C_{KC} is the Kozeny coefficient, Γ is the hydraulic tortuosity, which can be

72   defined as the ratio of the average length of the fluid paths to the geometric length of

73   the porous media (Matyka et al., 2008), and S is the specific surface area.

74   To predict the permeability properly, many different forms of modified KC

75   equations have been developed. Koponen (Koponen et al., 1996) proposed the

76   concept of effective porosity, which is defined as the ratio of the volume of the

77   conducting pores to the total pore volume, to replace the original porosity in Eq. 1. He

78   considered that some pores were interconnected and contributed very little or nothing

79   to the global flow. Later, Koponen (Koponen et al., 1997) used the lattice-gas cellular

80   automaton method to simulate an uncompressible flow in a 2D porous medium and

81   gave the relationship between effective porosity and original porosity. However,

82   compared to a 2D porous medium, the structure of a 3D porous medium is more

83   complicated. 2D simulations cannot consider the real pore connectivity. The empirical

84   formula of the 2D model is not practical. Sheikh (Sheikh and Pak, 2015) gave a new

85   empirical formula of the effective porosity for 3D conditions using the lattice

86 Boltzmann method. However, some parameters for his empirical formula are not

87 easily obtained.

88 The geometric characteristic is also a key factor that influences the permeability

89 of the pore medium. Some researchers have used regularly arranged spheres or

90 cylinders (Li et al., 2005; Okabe and Blunt, 2004), whereas others have used random

91 packed methods (Lee and Yang, 1997; Maier et al., 1998) to build porous media with

92 simple geometric features to study permeability. Their results have shown that

93 different arrangements of particles can cause different permeabilities. Some studies of

94 the influence of particle shape on the permeability of a porous medium through

95 numerical simulations have been carried out in the past (Dorai et al., 2015; Osiptsov,

96 2017; Saomoto and Katagiri, 2015; Scholes et al., 2007; Stewart et al., 2006). These

97 studies used regularly shaped particles such as cubes or ellipsoids. Chukwudozie

98 (Chukwudozie and Tyagi, 2013) simulated the effect of the surface geometric

99 characteristics of particles on permeability. In their study, the surface geometric

100 characteristics of particles were controlled by the several bulges above the sphere, and

101 the particle arrangement in the porous medium was cubic and centred as a regular

102 body, which is very different from the real arrangement condition. Natural soil

103 particles can be regarded as a set of spheres with a random size distribution that

104 reflect realistic conditions. Liu (Liu and Jeng, 2019) used two parameters (Wadell

105 sphericity and Cox roundness) to express the roughness of spherical particles. Their

106 simulation results showed that the sensitivity of sphericity and roundness is less than

107 that of particle size distribution and porosity.

108   In previous studies, simulations have mainly focused on uniform particle size.

109   However, soil is composed of various particle sizes. Smaller particles may have more

110   influence on permeability due to their greater specific surface area (Ghassemi and Pak,

111   2011), so the size distribution of particles must be considered (Wilson et al., 2008). In

112   summary, although there are many formulas for predicting permeability using

113   geometric parameters, only a few can be used in engineering practice. The empirical

114   formulas proposed in the existing studies are diverse, lack a general format, and can

115   be applied only to special soils.

116   Previous studies have mainly focused on investigating the permeability of

117   laminar flow through porous media while neglecting the characteristics of turbulent

118   flow. This is mainly because of the complexities of the flow field in porous media and

119   the significant computational resources required for simulating turbulence. However,

120   understanding the behaviour of turbulent flow is crucial. Fattahi (Fattahi et al., 2016)

121   employed a lattice Boltzmann method to investigate high Reynolds number flow

122   through an unstructured packing of spherical particles, but a comprehensive analysis

123   of the permeability regularities was not conducted. In this study, we present a

124   three-dimensional numerical simulation using a multiple relaxation time lattice

125   Boltzmann method to examine the flow through a soil medium composed of rigid

126   spherical particles with a certain size distribution. Through numerical simulations, we

127   establish correlations between parameters such as porosity, particle size distribution,

128   Reynolds number, and permeability.

129   Many researchers have used numerical simulation methods to study porous

130 media (Bogdanov et al., 2003; Hasanov et al., 2020). Traditional numerical simulation

131 methods cannot manage the complex boundary conditions of porous media. The

132 lattice Boltzmann method (LBM) proposed by McNamara and Zanetti (McNamara

133 and Zanetti, 1988) is a mesoscopic simulation method that combines macroscopic

134 continuous simulation and microscopic molecular dynamics simulation. It is a

135 conventional approach used to simulate the seepage of porous media. In addition to

136 the lattice Boltzmann method, some researchers have used the finite volume method

137 (FVM) to study permeability at the pore scale (Garcia et al., 2009; Stefansson and

138 Keilegavlen, 2023; Torskaya et al., 2014). The disadvantage of the finite volume

139 method is that the general simulation conditions are relatively sparse because of the

140 complexity of FVM modelling. Furthermore, owing to the high computational

141 resource cost of solving the Navier–Stokes (N–S) equations, most of these studies

142 have employed calculations based on the Laplace equation instead of the N–S

143 equations.

144   The following work is structured as follows: Section 2 presents the numerical

145 model, which is divided into two parts: the lattice Boltzmann method (Section 2.1)

146 and the construction of porous media (Section 2.2). The validation of the presented

147 numerical model is discussed in Section 2.3. Section 3 provides a comparison of the

148 numerical results. Finally, Section 4 presents the conclusions of this study.

149

150 **2. Numerical Model and Validation**

151 **2.1 Lattice Boltzmann method for fluid flows**

152   The LBM is a conventional computational fluid method based on the lattice gas

153   automaton method and the Boltzmann equation. This method is a mesoscopic

154   simulation method and has a clear physical background based on molecular dynamics

155   theory. The advantage of the LBM in seepage problems lies with its strong capability

156   to simulate complex pore structures (Chen and Doolen, 1998).

157   The Bhatnagar–Gross–Krook (BGK) model is the most popular LB method with

158   a standard bounce-back scheme for fluid–solid boundary conditions (Guo et al., 2000).

159   In the BGK model, the collision operator is approximated by a single relaxation time

160   (SRT) approximation. However, the SRT approximation has some disadvantages, such

161   as numerical instability and viscosity dependence at boundary locations. The

162   dependence on viscosity causes some problems in seepage simulations. The

163   permeability becomes viscosity dependent, even though it should be a physical

164   property of the porous medium alone. By using a multiple relaxation time (MRT)

165   approach, which separates the relaxation times for different kinetic nodes, the

166   disadvantage of the BGK model can be significantly overcome to improve numerical

167   stability (Du et al., 2006; Pape et al., 2000). The general form of the governing

168   equation with the D3Qq velocity set in the MRT model is as follows:

169
$$f_\alpha\left(\mathbf{x}+\mathbf{e}_a\Delta t, t+\Delta t\right)-f_\alpha\left(\mathbf{x},t\right)=-\mathbf{M}^{-1}\left[\mathbf{S}\left(\mathbf{m}-\mathbf{m}^{eq}\right)\right] \tag{4}$$

170   where $f_\alpha\left(\mathbf{x},t\right)$ denotes the density distribution function at lattice position x and time

171   t; $\mathbf{e}_a$ is the discrete velocity in the α direction, and α ranges from 1 to q-1 in three

172   dimensions. The particle speed is c=$\Delta x/\Delta t$, Δx is the lattice constant, and Δt is the time

173   step. $\mathbf{M}$ is the transformation matrix. $\mathbf{S}$ is the diagonal collision matrix in moment

174 space. **m** is the vector of moments. $\mathbf{m}^{eq}$ is the vector of equilibrium moments.

175   The equilibrium distribution function of the D3Q27 model is

176
$$f_\alpha^{eq} = \omega_\alpha \rho + \omega_\alpha \rho_0 \left[\frac{\mathbf{e}_\alpha \cdot \mathbf{u}}{c_s^2} + \frac{(\mathbf{e}_\alpha \cdot \mathbf{u})^2}{2c_s^4} - \frac{|\mathbf{u}|^2}{2c_s^2} \right] \tag{5}$$

177 where c_s is the lattice sound speed ($c_s^2 = c^2/3$), ρ_0 is the reference density of the fluid

178 and ω_α is the weight coefficient, which has the following value:

179
$$\omega_0 = \frac{8}{27}, \ \omega_{1-6} = \frac{2}{27}, \ \omega_{7-18} = \frac{1}{54}, \ \omega_{19-26} = \frac{1}{216} \tag{6}$$

180   The macro density and velocity can be obtained through the distribution

181 function:

182
$$\rho = \sum_\alpha f_\alpha \tag{7}$$

183
$$\rho_0 \mathbf{u} = \sum_\alpha f_\alpha \mathbf{e}_\alpha \tag{8}$$

184 where ρ is the fluid density and **u** is the vector of fluid velocity.

185   Eq. (2) can be restored to the Navier–Stokes equation based on the Chapman–

186 Enskog expansion (Liu et al., 2021).

187   The Smagorinsky eddy viscosity model (Krafczyk and Olke, 2003) is used to

188 simulate turbulent flows, and then the LBE large eddy simulation (LES) model is

189 established. The eddy viscosity υ_t is calculated by the mean strain rate $\bar{\mathbf{S}}$,

190
$$\upsilon_t = (C_s \Delta)^2 \|\bar{\mathbf{S}}\| \tag{9}$$

191 where $C_s = 0.15$ is the Smagorinsky constant, $\Delta = \delta_x$ is the filter length, and

192 $\|\bar{\mathbf{S}}\| = \sqrt{2\bar{S}_{ij}\bar{S}_{ij}}$.

193   In the LBE, the mean strain rate $\bar{\mathbf{S}}$ is calculated by the nonequilibrium part of

194 the mean second-order moment $\bar{\bar{\Pi}}$:

195
$$\bar{S}_{ij} = \frac{3\bar{\Pi}_{ij}}{-2\tau_{total}\rho_0 c^2 \delta_t} \qquad (10)$$

196 where $\bar{\Pi}_{ij} = \sum_{\alpha=0}^{q-1} \mathbf{e}_{\alpha i}\mathbf{e}_{\alpha j}f_\alpha - \rho_0 u_i u_j - p\delta_{ij}$.

197   In our simulations, the pressure gradient boundary condition is applied to the

198 inlet and outlet boundary. On the solid–fluid surface, the central linear interpolation

199 (CLI) scheme of boundary conditions is applied. The CLI scheme was proposed by

200 Ginzburg (d'Humières et al., 2002; Ginzburg et al., 2008; Ginzburg and d'Humières,

201 2003) based on two relaxation times (TRT), which can be seen as the minimal

202 configuration that provides just enough free relaxation parameters to avoid nonlinear

203 dependencies of the truncation errors on the viscosity in the context of porous media

204 simulations.

205   Let $\mathbf{x}_{f_i}$ denote a lattice node located at a distance of at most $i > 0$ cells from the

206 boundary, and let $q = \left|\mathbf{x}_{f_1} - \mathbf{x}_w\right| / \left|\mathbf{x}_{f_1} - \mathbf{x}_b\right|$ define a normalized wall distance (Fig. 1).

207 The CLI scheme requires three values at two fluid nodes. The CLI scheme can be

208 expressed as

209
$$f_\beta(\mathbf{x}_{f1},t) = \frac{1-2q}{1+2q}f_\alpha(\mathbf{x}_{f1},t) - \frac{1-2q}{1+2q}f_\beta(\mathbf{x}_{f1}-\mathbf{e}_\alpha\delta_t,t) + f_\alpha(\mathbf{x}_{f1}+\mathbf{e}_\alpha\delta_t,t) \qquad (11)$$

210 where β is the diametrically opposite direction to α.

211   To verify the developed MRT–LBM model and the given boundary conditions,

212 the Poiseuille flow between two parallel plates is simulated. Between the two parallel

213 plates, the velocities at the plates are zero, and the velocity reaches its maximum in

214 the middle. The velocity profile between two plates of width $2a$ is a parabolic curve

215 given by

216
$$u(y) = \frac{\Delta p}{2v\rho L}\left(a^2 - y^2\right) \tag{12}$$

217 where L is the length along the low direction, v is the fluid dynamic viscosity, Δp is

218 the pressure difference, and y is the distance of any point from the middle of the

219 domain.

220   The maximum velocity along the centreline is given by

221
$$u_0 = \frac{\Delta p a^2}{2v\rho L} \tag{13}$$

222   The lattice sizes of the calculation domain are set to $100 \times 100 \times 200$, and the

223 Reynolds number is 0.1, which indicates that the flow is laminar. The velocity contour

224 and the comparison between the numerical results and analytical solutions of the

225 velocity in the x direction are shown in Fig. 2.

226

227 **2.2 Simulation of porous medium**

228   Simulation methods for forming granular packings of hard particles usually

229 involve one of two methods. One is the concurrent algorithm, which involves the

230 densification of a fixed number of particles. The other is the sequential algorithm,

231 which involves progressively adding more particles to a fixed volume.

232   The sphere packing code utilizes the concurrent algorithm used by Williams and

233 Philipse to generate packings of spherocylinders (Williams and Philipse, 2003). The

234 algorithm has been modified to support the generation of packings for systems of

235 spheres with lognormally distributed radii and to provide control over the final

236 porosity of the packing. The major steps can be seen in Fig. 3.

237   To improve convergence, the spheres are divided into a collection of cells

238   consisting of equally sized subdomains, which is a common optimization for

239   N-particle methods. To consider potential overlaps only from neighbouring cells for a

240   given sphere, the code is significantly accelerated by increasing the number of cells,

241   thereby reducing the length of the search path needed when computing overlaps.

242   However, this optimization can lead to oversights in overlap computation if the

243   maximum radius exceeds half of the cell width. Errors may occur if too many cells are

244   requested for a given system, causing the maximum radius to exceed half of the cell

245   width. Nonetheless, the generated porous medium is consistent with the actual on-site

246   conditions. Fig. 4 illustrates the typical porous media constructed in the study.

247   **2.3 Simulation of seepage in the porous medium**

248   The boundary conditions in the simulation domain are set as follows: the

249   pressure boundary condition is used for the inlet boundary and the outlet boundary.

250   The CLI scheme boundary condition (Ginzburg et al., 2008; Ginzburg and

251   d'Humières, 2003) is used for the other four boundaries and the boundaries of the

252   solid particles. The simulation domain is set to 200×200×200, and the porosity ε is

253   0.5.

254   The relative permeability can be calculated by Eq. 1. The dimensionless

255   permeability k is defined as

256    $$k = \frac{K}{d_p{}^2} \tag{14}$$

257   where d_p is the characteristic length of the spherical particles. For the seepage of

258 porous media, the medium particle size d_{50} is generally used to denote the

259 characteristic length.

260   For the Poiseuille flow between two parallel plates filled with a porous medium

261 of porosity ε, the Navier–Stokes equation can be simplified as

$$\frac{\nu}{\varepsilon}\frac{\partial^2 u}{\partial y^2}+\frac{\mathbf{F}}{\varepsilon}=0 \qquad (15)$$

262

263 where $\mathbf{F}$ denotes the total body force due to the porous media and other external force

264 fields and is given by

$$\mathbf{F}=-\frac{\varepsilon\nu}{K}\mathbf{u}-\frac{\varepsilon F_\varepsilon}{\sqrt{K}}|\mathbf{u}|\mathbf{u}+\varepsilon\mathbf{G} \qquad (16)$$

265

266 where $\mathbf{G}$ is the body force induced by the external force. F_ε is the geometric function

267 and is related to the porosity ε. On the right side of Eq. 16, the first term is the linear

268 (Darcy) and the second term is the nonlinear (Forchheimer) drag due to the porous

269 medium.

270   The velocity of the solid–fluid boundary is zero, and the lateral velocity

271 component v is zero everywhere. The quadratic nature of the nonlinear drag makes it

272 negligible for low-velocity flows. For the cases in which the Reynolds number is

273 small, the nonlinear drag can be neglected. Without the nonlinear term, the analytical

274 solution of Eq. 15 can be written as

$$u=\frac{GK}{\nu}(1-\frac{\cosh[r(y-H/2)]}{\cosh(rH/2)}) \qquad (17)$$

275

276 where u_0 is the peak velocity of the flow along the centreline given by

$$u_0=\frac{GK}{\nu}[1-\cosh^{-1}(\frac{rH}{2})] \qquad (18)$$

277

278   where $r = \sqrt{\nu / K}$.

279   Due to the presence of solid particles, the velocity distribution of a single line

280   may deviate from the analytical solution. Therefore, to more accurately compare with

281   the analytical solution, the mean velocity of the cross section at height *y* is calculated

282   as a replacement for the local velocity at that particular location. The comparison

283   between the numerical results and analytical solutions of the velocity in the *y*

284   direction is shown in Fig. 5(a). The analytical solutions are calculated by Eq. 18, and

285   the simulation results are the mean velocity of the cross section in the height *y*.

286   Because of the randomness of the sphere pack structure, the mean velocity

287   distribution of the porous seepage may not fit the analytical solutions accurately. The

288   maximum error of the velocity is 10.6%.

289   Fig. 5(b) shows the streamlines of the simulated porous medium. In pore spaces,

290   streamlines often undergo changes, particularly in the regions between large and small

291   particles. Between large particles, streamlines tend to become more tortuous and

292   complex, as the large particles impede fluid flow and cause streamlines to bend and

293   branch. Between small particles, streamlines tend to become smoother and more

294   linear, as the gaps between small particles are smaller and fluid can more easily pass

295   through these gaps and flow along relatively straight paths.

296   Sobieski (Sobieski and Trykozko, 2014) calculated the permeability and

297   Forchheimer coefficient based on experimentally measured flow rates and pressure

298   drops. Fig. 6 illustrates the comparison of the velocity–pressure relationship between

299   the experimental data and simulation data. The simulation data are in good agreement

14

300 with the experimental data. The simulation parameters are based on Sobieski's

301 experiment and are summarized in Table 1. The maximum error between the

302 simulation results and experimental results is 6%. The main reason for the error is

303 attributed to the unclear characteristics of certain porous media, such as the

304 nonuniform coefficient.

305

306 **2.4 Mesh sensitivity analysis**

307 The minimum resolution of each spherical particle required for simulation

308 accuracy needs to be determined. Under the situation of porosity $\varepsilon = 0.5$, the

309 permeability of spherical particles with different resolutions (d_p/dx) is shown in Fig. 7.

310 Fig. 7 illustrates that when the diameters of medium spherical particles reach ten

311 lattices, the dimensionless permeability will remain stable. Twenty lattices are

312 sufficient to describe the structure of spherical particles.

313

314 **3. Results and Discussion**

315 **3.1 Effect of porosity on permeability**

316 To study the effect of porosity on permeability, it is necessary to ensure that other

317 parameters remain unchanged. The porosity is adjusted by controlling the number of

318 particles, and the floc size distribution remains unchanged. The medium floc diameter

319 was fixed at 20 lattice units, and the particle numbers were set to 1000. Considering

320 the porosity of natural soil, the upper limit of porosity was set to 0.55. Nine porous

321 media with different porosities varying from 0.35 to 0.55 were constructed. Their

322   permeabilities were simulated and calculated.

323   The widely used form of the KC equation is obtained as (Chen and Doolen,

324   1998)

325
$$K = \frac{\varepsilon^3}{(1-\varepsilon)^2} \frac{d_p^2}{180} \qquad (19)$$

326   Sheikh (Sheikh and Pak, 2015) summarized another equation, which after some

327   substitutions becomes

328
$$K = \frac{1-1.209(1-\varepsilon)^{2/3}}{60\varepsilon} \frac{\varepsilon^3}{(1-\varepsilon)^2} d_p^2 \qquad (20)$$

329   Recently, Ahmadi (Ahmadi et al., 2011) provided the following relationship by

330   analytical derivation:

331
$$K = \frac{1-1.209(1-\varepsilon)^{2/3}}{30[1-1.209(1-\varepsilon)^{2/3}+2\varepsilon]} \frac{\varepsilon^3}{(1-\varepsilon)^2} d_p^2 \qquad (21)$$

332   Jeong's equation (Jeong, 2010) is as follows:

333
$$K = e^{(0.709\ln(\varepsilon^{11/3}/(1-\varepsilon)^2)-5.09)} d_p^2 \qquad (22)$$

334   The abovementioned formula is mainly derived mathematically, often making

335   simplified assumptions about the porous medium model. As a result, there may be

336   some deviation from the actual results.

337   Based on the calculated results of the permeability (Fig. 8), the correlation

338   between the permeability and porosity of the porous media was determined.

339   According to the KC equation (Eq. 19), a linear regression on the relative

340   permeability K and the expression $\varepsilon^3/(1-\varepsilon)^2$ of the porosity was performed. As

341   shown in Fig. 9（a）, R^2 is 0.9876. The largest relative error is 50% when the porosity

342   is 0.35.

343   To reduce the relative error and obtain a more accurate correlation between

344   permeability and porosity, the logarithms of the relative permeability K and

345    $\varepsilon^3/(1-\varepsilon)^2$ were taken separately, and linear regression was performed to obtain the

346   results shown in Fig. 9(b). The R^2 is 0.9951, which indicates a good degree of fitting.

347   In this study, a new fitting formula is introduced on the basis of the KC formula. The

348   fitting curve is shown in Fig. 10.

349
$$K = (\frac{\varepsilon^3}{(1-\varepsilon)^2})^{0.76}\frac{d_p^{\,2}}{80} \tag{23}$$

350

351   **3.2 Effect of particle size distribution on permeability**

352   Soil is composed of particles with different sizes. Smaller particles may have

353   more influence on the permeability due to their greater specific surface area (Liu and

354   Jeng, 2019). Hence, additional investigations have been conducted on correlating the

355   permeability with the particle size distribution. The particle size distribution can be

356   characterized by the gradation parameters. The coefficient of nonuniformity C_u, which

357   reflects the distribution of different particle sizes, can be expressed as

358
$$C_u = d_{60}/d_{10} \tag{24}$$

359   To examine the influence of the coefficient of nonuniformity on the permeability,

360   six porous media with different gradation parameters were constructed, and their

361   porosity ε was set to 0.5. The gradation curves for the six porous media are shown in

362   Fig. 11. The relationship between the coefficient of nonuniformity and the relative

363   permeability coefficient is shown in Fig. 12 when the flow is laminar. The results

364 show that the permeability depends on the coefficient of nonuniformity and increases

365 with an increasing coefficient of nonuniformity, almost with a parabolic trend.

366 Therefore, the effect of the particle size distribution on the permeability is obvious.

367 Equation 25 accounts for the influence of the particle size distribution in the modified

368 KC formula.

369
$$K = C_1 (\frac{\varepsilon^3}{(1-\varepsilon)^2})^{0.76} d_p^{\ 2} \tag{25}$$

370 where C_1 is a coefficient related to the coefficient of nonuniformity. It can be

371 expressed separately as

372
$$C_1 = 0.014 C_u^{\ 2} - 0.03 C_u + 0.022 \tag{26}$$

373

374 **3.3 Effect of the Reynolds number on permeability**

375 Turbulent flow significantly affects the rate of transport. It comprises a complex

376 flow pattern with various scales of vortices and turbulence structures. This flow state

377 enhances the transport rate within the medium by facilitating mixing and diffusion

378 mechanisms, thereby promoting rapid substance transfer between different regions.

379 Hence, studying turbulent flow helps us better comprehend and control the

380 permeation rate of substances.

381 The particle Reynolds number (Re) for flow through a porous medium is

382 typically expressed as

383
$$Re = \frac{VD}{v} \tag{27}$$

384 where D is the medium diameter of the porous medium particles.

18

385   Flow through soil with a particle Reynolds number less than 1 is classified as

386   laminar, while flow with a particle Reynolds number greater than 100 is considered

387   turbulent. Flow that falls between these two limits is transient. In this study, several

388   simulations were conducted with varying particle Reynolds numbers in the range of

389   0.001 to 3,000 (0.001, 0.01, 001, 0.3, 30, 100, 300, and 3000). Figure 13 demonstrates

390   that the dimensionless permeability remains constant in the laminar regime and does

391   not vary as the particle Reynolds number increases. However, as the particle Reynolds

392   number enters the transient regime, the dimensionless permeability decreases. This

393   finding is consistent with the conclusions drawn in Fattahi's research (Fattahi et al.,

394   2016). Therefore, the empirical formula of permeability needs to consider the effect of

395   the Reynolds number.

396   The Forchheimer term (Eq. 2) is commonly employed to describe the impact of

397   nonlinear drag in turbulent flow. The Forchheimer coefficient β is an empirical

398   coefficient that relies on soil and flow characteristics. The commonly used empirical

399   formula of the Forchheimer coefficient β can be written as

400
$$\beta = \beta_0 \times \frac{1-\varepsilon}{\varepsilon^3} \times \frac{1}{d_{50}}$$
(28)

401   where β_0 is an empirical parameter.

402   In previous studies, researchers did not account for the variation in the

403   Forchheimer coefficient with the Reynolds number. Based on Eq. 2, the Forchheimer

404   coefficient β can be calculated. Fig. 14 demonstrates the relationship between the

405   particle Reynolds number and the Forchheimer coefficient. As the velocities increase,

406   the Forchheimer coefficient decreases. The fitting formula of the Forchheimer

407   coefficient is provided below:

408 $$\beta = (-0.006\ln(Re_p) + 0.051) \times \frac{1-\varepsilon}{\varepsilon^3} \times \frac{1}{d_{50}}$$ (29)

409   Under turbulent conditions, the fluid demonstrates an irregular velocity

410   distribution and exhibits vortex structures accompanied by highly intricate streamlines.

411   The irregularity of turbulence leads to significant variations in path and velocity as the

412   fluid traverses the pores of the medium, resulting in relatively low permeability.

413   On the other hand, laminar flow describes an ordered and parallel flow state of

414   the fluid within a porous medium. In laminar flow, the fluid displays a layered and

415   parallel velocity distribution with relatively regular streamlines. The ordered nature of

416   laminar flow results in minimal changes in path and velocity as the fluid passes

417   through the medium's pores, leading to relatively high permeability.

418   Based on the above conclusion, a modified Darcy formula considering the size

419   distribution of particles and particle Reynolds number is finally presented. When the

420   particle Reynolds number is less than 1, which indicates that the flow is laminar, Eq.

421   30 is applicable.

422 $$-\frac{dP}{dx} = \frac{1}{K} \cdot (\mu \cdot V)$$ (30)

423 $$K = C_1 \left(\frac{\varepsilon^3}{(1-\varepsilon)^2}\right)^{0.76} d_p{}^2$$ (31)

424   where C_1 is a coefficient related to the coefficient of nonuniformity. It can be

425   expressed separately as

426 $$C_1 = 0.014C_u{}^2 - 0.03C_u + 0.022$$ (32)

427   When the particle Reynolds number is greater than 1, which indicates that the

428   flow gradually becomes turbulent, Eq. 33 is applicable. K refers to the same value as

429   Eq. 31.

430
$$-\frac{dP}{dx} = \frac{1}{K} \cdot (\mu \cdot V) + \beta \cdot (\rho \cdot V^2)$$
(33)

431
$$\beta = (-0.006\ln(Re_p) + 0.051) \times \frac{1-\varepsilon}{\varepsilon^3} \times \frac{1}{d_{50}}$$
(34)

432   **4. Conclusions**

433   A newly developed 3D multiple relaxation time LBM code has been employed to

434   investigate the effects of several issues, such as effective porosity, particle size,

435   particle size distribution and the particle Reynolds number, on the permeability of

436   porous media. Many numerical simulations were performed under different conditions.

437   From the LBM simulations conducted in this study, the following conclusions can be

438   drawn:

439   (1) The effects of porosity, particle size, particle size distribution and Reynolds

440   number on the permeability were studied in this paper. It was proven that in addition

441   to the influence of porosity and particle size distribution on the permeability, the

442   influence of the Reynolds number on the permeability is obvious and cannot be

443   ignored.

444   (2) An analysis of the seepage flow field at the pore scale revealed that certain

445   seepage channels within the network exhibit significantly higher velocities than others,

446   indicating the presence of a dominant seepage main channel phenomenon in the

447   network.

448   (3) Based on the numerical simulation results, a modified Darcy formula

449   considering all the factors was provided.

450   The permeability coefficient formula is a valuable tool for future simulations of

451   macroscopic porous seepage models. By integrating this coefficient into numerical

452   models or simulations, we can effectively simulate and analyse the fluid behaviour

453   within porous media under different conditions.

454

461

462   **Data Availability Statement**

463   The data for the results presented is available, and the results can be reproduced,

464   using a Docker container available at https://dx.doi.org/10.5281/zenodo.10005571

465   (Zhang & Li, 2023)

466

467   **References**

468   Ahmadi, M.M., Mohammadi, S., Hayati, A.N., (2011). Analytical derivation of

469   tortuosity and permeability of monosized spheres: A volume averaging approach.

Physical Review E, 83, 026312. https://doi.org/10.1103/PhysRevE.83.026312

Bogdanov, I.I., Mourzenko, V. V., Thovert, J.F., Adler, P.M., (2003). Effective permeability of fractured porous media in steady state flow. *Water Resources Research*, 39, 1-13. https://doi.org/10.1029/2001WR000756

Carman, P.C., (1939). Permeability of saturated sands, soils and clays. *The Jou rnal of Agricultural Science*, 29(2), 262–273. https://doi.org/10.1017/S00218 59600051789

Carman, P. C. (1997). Fluid flow through granular beds. *Chemical Engineering Research and Design*, 75, S32–S48. https://doi.org/10.1016/S0263-8762(97)80 003-2

Chen, S., Doolen, G.D.,（1998). Lattice Boltzmann method for fluid flows. *Annua l Review of Fluid Mechanics*, 30, 329–364. https://doi.org/10.1146/annurev.flu id.30.1.329

Chukwudozie, C., Tyagi, M., (2013). Pore scale inertial flow simulations in 3-D s mooth and rough sphere packs using lattice Boltzmann method. *Transport Ph enomena and Fluid Mechanics*, 59, 4858–4870. https://doi.org/10.1002/aic.14 232

Despois, J.F., Mortensen, A., (2005). Permeability of open-pore microcellular mat erials. *Acta Materialia*, 53, 1381–1388. https://doi.org/10.1016/j.actamat.2004. 11.031

D'Humières, D., Ginzburg, I., Krafczyk, M., Lallemand, P., Luo, L.S., (2002). Mu ltiple-relaxation-time lattice Boltzmann models in three dimensions. *Mathema*

tical, Physical and Engineering Sciences, 360, 437–451. https://doi.org/10.109
8/rsta.2001.0955

Dorai, F., Moura Teixeira, C., Rolland, M., Climent, E., Marcoux, M., Wachs, A.,
(2015). Fully resolved simulations of the flow through a packed bed of cyli
nders: Effect of size distribution. *Chemical Engineering Science*, 129, 180–19
2. https://doi.org/10.1016/j.ces.2015.01.070

Du, R., Shi, B., Chen, X., (2006). Multi-relaxation-time lattice Boltzmann model
for incompressible flow. *Physics Letters A*, 359, 564–572. https://doi.org/10.1
016/j.physleta.2006.07.074

Fattahi, E., Waluga, C., Wohlmuth, B., Rüde, U., Manhart, M., Helmig, R., (201
6). Lattice Boltzmann methods in porous media simulations: From laminar to
turbulent flow. *Computers & Fluids*, 140, 247–259. https://doi.org/10.1016/j.
compfluid.2016.10.007

Garcia, X., Akanji, L.T., Blunt, M.J., Matthai, S.K., Latham, J.P., (2009). Numeri
cal study of the effects of particle shape and polydispersity on permeability.
Physical Review E, 80, 021304. https://doi.org/10.1103/PhysRevE.80.021304

Ghassemi, A., Pak, A., (2011). Pore scale study of permeability and tortuosity
for flow through particulate media using Lattice Boltzmann method. *Intern
ational Journal for Numerical and Analytical Methods in Geomechanics*, 3
5, 886–901. https://doi.org/10.1002/nag.932

Ginzburg, I., d'Humières, D., (2003). Multireflection boundary conditions for la
ttice Boltzmann models. *Physical Review E*, 68, 066614. https://doi.org/10.1

103/PhysRevE.68.066614

Ginzburg, I., Verhaeghe, F., dHumières, D., (2008). Two-relaxation-time Lattice Boltzmann scheme: about parametrization, velocity, pressure and mixed bou ndary conditions. *Communications in Computational Physics*, 3, 427-478.

Guo, Z., Shi, B., Wang, N., (2000). Lattice BGK Model for Incompressible Na vier-Stokes Equation. *Journal of Computational Physics*, 165, 288–306. htt ps://doi.org/10.1006/jcph.2000.6616

Hasanov, A.K., Dugan, B., Batzle, M.L., (2020). Numerical Simulation of Oscil lating Pore Pressure Experiments and Inversion for Permeability. *Water Res ources Research*, 56, 1-16. https://doi.org/10.1029/2019WR025681

Koponen, A., Kataja, M., Timonen, J., (1996). Tortuous flow in porous media. *Physical Review E*, 54, 406–410. https://doi.org/10.1103/PhysRevE.54.406

Koponen, A., Kataja, M., Timonen, J., (1997). Permeability and effective porosi ty of porous media. *Physical Review E*, 56, 3319–3325. https://doi.org/10.1 103/PhysRevE.56.3319

Krafczyk, M., Tölke, J., Luo, L.S., (2012). Large-eddy simulations with a multi ple-relaxation-time LBE model. *International Journal of Modern Physics B*, 17, 33-39. https://doi.org/10.1142/S0217979203017059

Lee, S.L., Yang, J.H., (1997). Modeling of Darcy-Forchheimer drag for fluid fl ow across a bank of circular cylinders, *International Journal of Heat and Mass Transfer*, 40(13), 3149-3155. https://doi.org/10.1016/S0017-9310(96)00 347-X

25

536 Liu, G., Zhang, J., Zhang, Q., (2021). A high-performance three-dimensional lat

537   tice Boltzmann solver for water waves with free surface capturing. *Coastal*

538   *Engineering*, 165, 1-23. https://doi.org/10.1016/j.coastaleng.2021.103865

539 Li, Y., LeBoeuf, E.J., Basu, P.K., Mahadevan, S., (2005). Stochastic modeling

540   of the permeability of randomly generated porous media. *Advances in Wat*

541   *er Resources*, 28, 835–844. https://doi.org/10.1016/j.advwatres.2005.01.007

542 Liu, Y.F., Jeng, D.S., (2019). Pore scale study of the influence of particle geo

543   metry on soil permeability. *Advances in Water Resources*, 129, 232–249. ht

544   tps://doi.org/10.1016/j.advwatres.2019.05.024

545 Maier, R.S., Kroll, D.M., Kutsovsky, Y.E., Davis, H.T., Bernard, R.S., (1998).

546   Simulation of flow through bead packs using the lattice Boltzmann method.

547   *Physics of Fluids*, 10, 60–74. https://doi.org/10.1063/1.869550

548 Matyka, M., Khalili, A., Koza, Z., (2008). Tortuosity-porosity relation in porous

549   media flow. *Physical Review E*, 78(2), 026306. https://doi.org/10.1103/PhysRe

550   vE.78.026306

551 McNamara, G.R., Zanetti, G., (1988). Use of the Boltzmann equation to simulate

552   Lattice-Gas Automata. *Physical Review Letters*, 61, 2332–2335. https://doi.or

553   g/10.1103/PhysRevLett.61.2332

554 Okabe, H., Blunt, M.J., (2004). Prediction of permeability for porous media rec

555   onstructed using multiple-point statistics. *Physical Review E*, 70(6), 066135.

556   https://doi.org/10.1103/PhysRevE.70.066135

557 Osiptsov, A.A., (2017). Hydraulic fracture conductivity: effects of rod-shaped

26

proppant from lattice-Boltzmann simulations and lab tests. *Advances in Water Resources*, 104, 293–303. https://doi.org/10.1016/j.advwatres.2017.04.003

Pape, H., Clauser, C., Iffland, J., (2000). Variation of Permeability with Porosity in Sandstone Diagenesis Interpreted with a Fractal Pore Space Model. *Pure and Applied Geophysics*, 157, 603-619. https://doi.org/10.1007/PL00001110

Rodríguez, E., Giacomelli, F., Vazquez, A., (2004). Permeability-porosity relations hip in RTM for different fiberglass and natural reinforcements. *Journal of Co mposite Materials*, 38, 259–268. https://doi.org/10.1177/0021998304039269

Saomoto, H., Katagiri, J., (2015). Particle Shape Effects on Hydraulic and Electri c Tortuosities: A Novel Empirical Tortuosity Model Based on van Genuchten -Type Function. *Transport in Porous Media*, 107, 781–798. https://doi.org/10.1007/s11242-015-0467-z

Scholes, O.N., Clayton, S.A., Hoadley, A.F.A., Tiu, C., (2007). Permeability ani sotropy due to consolidation of compressible porous media. *Transport in P orous Media*, 68, 365-387. https://doi.org/10.1007/s11242-006-9048-5

Sheikh, B., Pak, A., (2015). Numerical investigation of the effects of porosity and tortuosity on soil permeability using coupled three-dimensional discrete -element method and lattice Boltzmann method. *Physical Review E*, 91(5), 053301. https://doi.org/10.1103/PhysRevE.91.053301

Sobieski, W., Trykozko, A., (2014). Darcy's and Forchheimer's laws in practice. Part 1. The experiment, Technical Sciences, 17(4), 321-335.

Stefansson, I., Keilegavlen, E., (2023). Numerical Treatment of State-Dependent P

580   ermeability in Multiphysics Problems. *Water Resources Research*, 59, 1-14. h

581   ttps://doi.org/10.1029/2023WR034686

582 Stewart, M.L., Ward, A.L., Rector, D.R., (2006). A study of pore geometry eff

583   ects on anisotropy in hydraulic permeability using the lattice-Boltzmann m

584   ethod. *Advances in Water Resources*, 29, 1328–1340. https://doi.org/10.1016

585   /j.advwatres.2005.10.012

586 Torskaya, T., Shabro, V., Torres-Verdín, C., Salazar-Tio, R., Revil, A., (2014).

587   Grain shape effects on permeability, formation factor, and capillary pressur

588   e from pore-scale modeling. *Transport in Porous Media*, 102, 71–90. https:

589   //doi.org/10.1007/s11242-013-0262-7

590 Williams, S.R., Philipse, A.P., (2003). Random packings of spheres and spheroc

591   ylinders simulated by mechanical contraction. *Physical Review E*, 67, 0513

592   01. https://doi.org/10.1103/PhysRevE.67.051301

593 Wilson, A.M., Huettel, M., Klein, S., (2008). Grain size and depositional envir

594   onment as predictors of permeability in coastal marine sands. *Estuarine, C*

595   *oastal and Shelf Science*, 80, 193–199. https://doi.org/10.1016/j.ecss.2008.06.

596   011

597

598

599

600

601

604   Table 1 Simulation Parameters Used in Section 2.3

Parameter	Value
Fluid density	994.49 kg/m^3
Dynamic viscosity coefficient	0.000743 kg/m·s
Kinematic viscosity coefficient	0.000000747m^2/s
Porosity of porous media	0.37
Medium particle size of porous media	1.95 mm
Nonuniformity coefficient	1.1
Water velocity range	0.00002-0.01 m/s

605

606
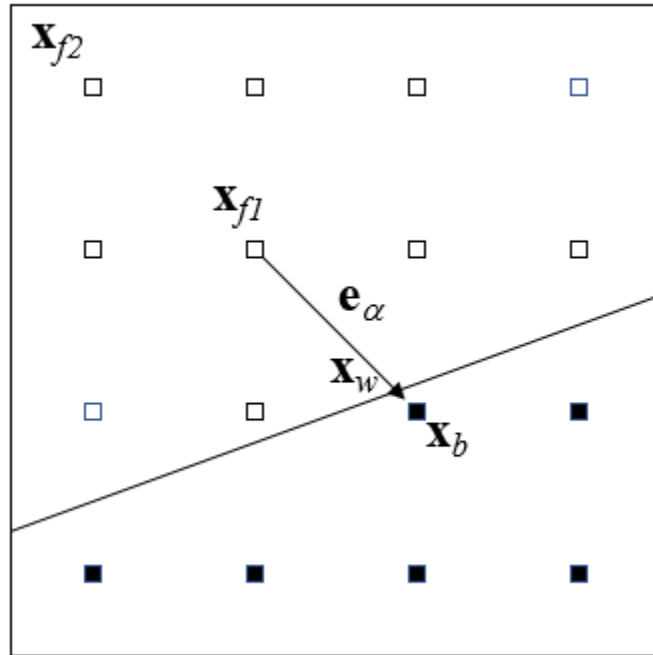
607   Fig. 1. A two-dimensional example of the boundary node, where $\mathbf{X}_f$ represents fluid

608   node and $\mathbf{X}_b$ represents solid node.

609

610
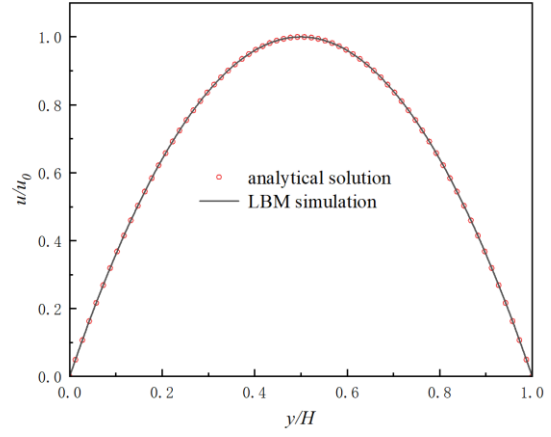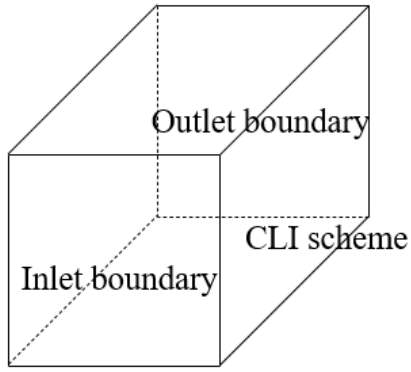
611   Fig. 2. (a) The simulation domain of the numerical model, where the inlet boundary

612   and outlet boundary using the pressure boundary condition. And the CLI boundary

613   condition is used for the other four boundaries. (b) Comparison between LBM

614   simulation and analytical solution of Poiseuille flow (Eq.13).

615
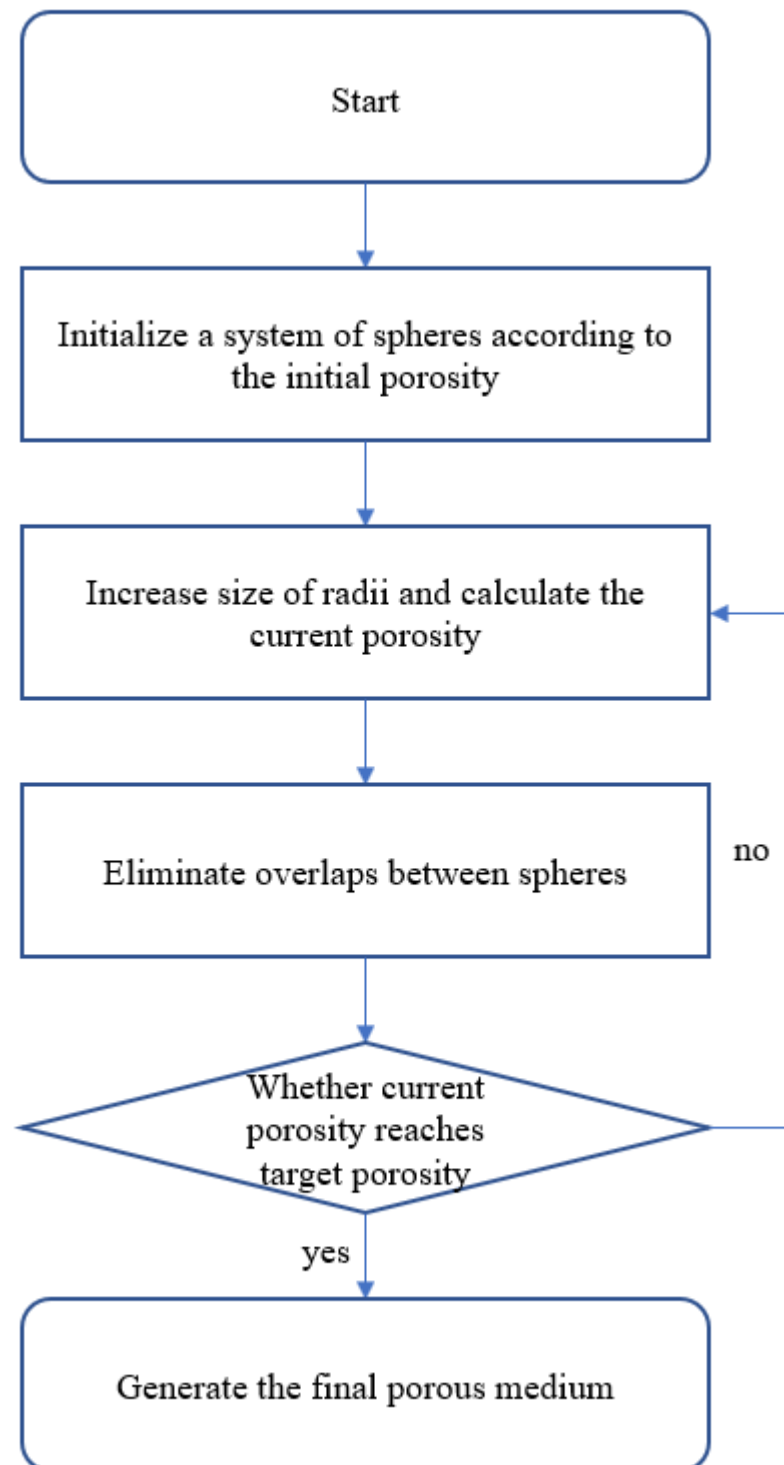
616
617   Fig. 3. Flowchart of the generation of porous medium

618
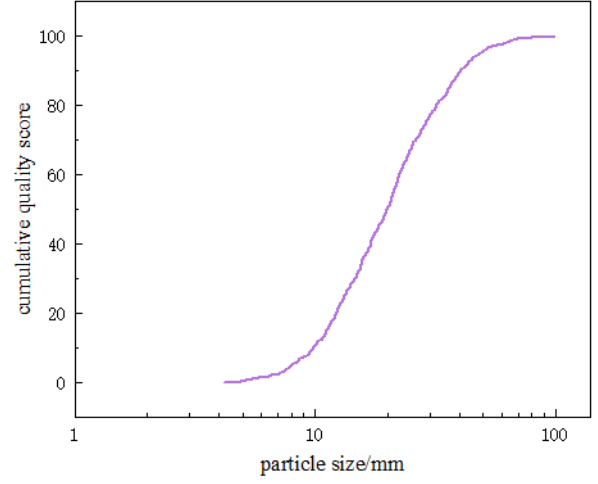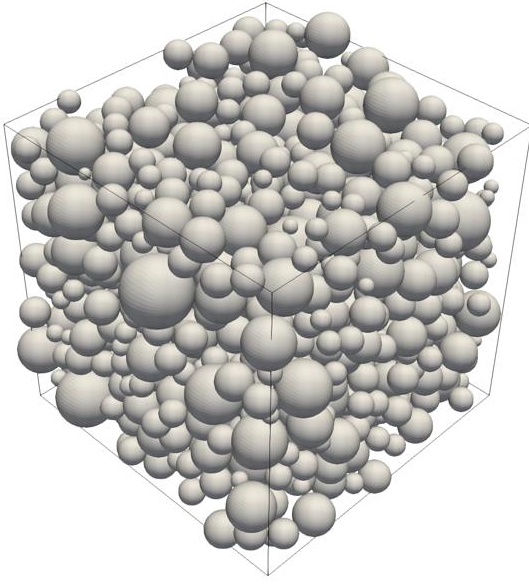
619

620   Fig. 4. (a) Porous medium is constructed using the code, where the porosity of porous

621   medium is 0.5 and the particle number is 1000. (b) Particle size distribution of the

622   generated porous medium.
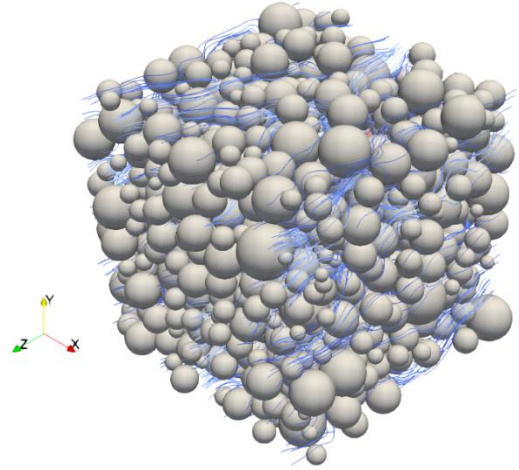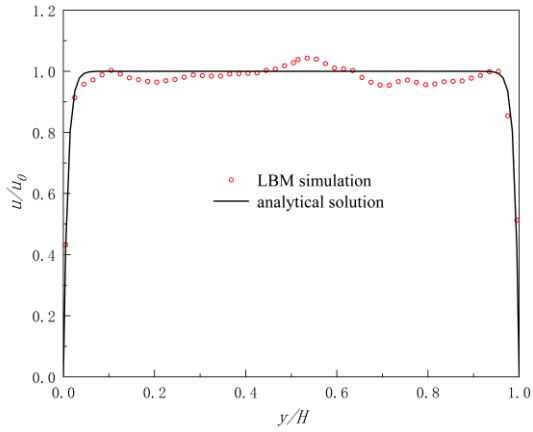
623

624   Fig. 5. (a) Comparison between LBM simulation and analytical solution of porous

625   Poiseuille flow (Eq.18) with porosity of 0.5.(b) Streamlines of flow through spherical

626　　　particles in porous Poiseuille flow

627
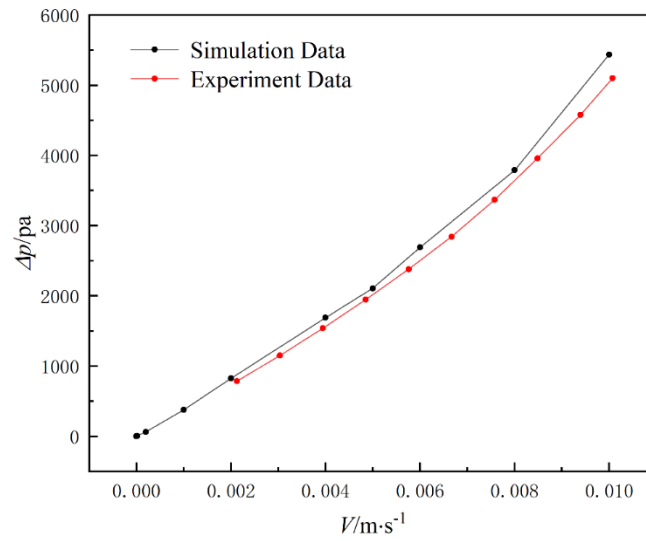
628　　Fig. 6. Comparison between experimental data by Sobieski and Trykozko (2014) and

629　　simulation data
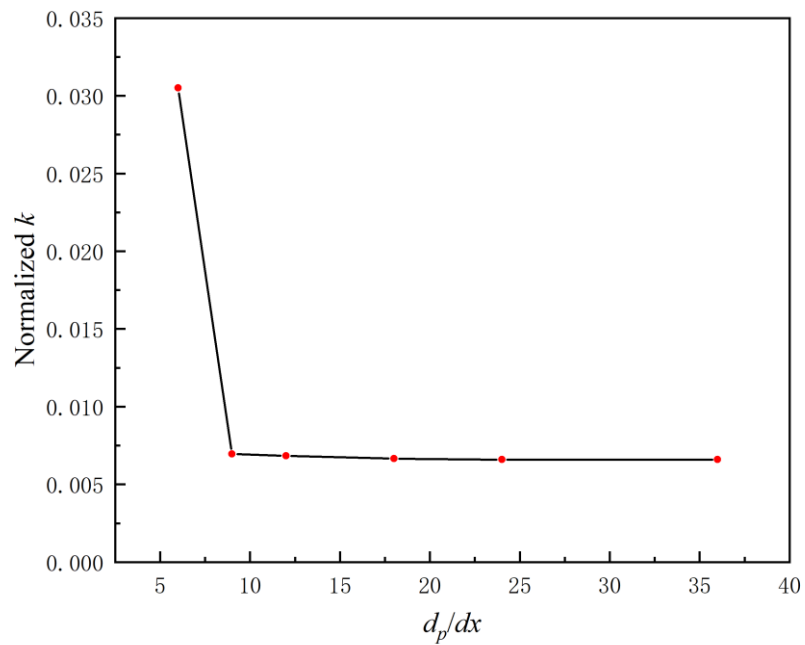
630

631　　Fig. 7. Permeability of spherical particles with different resolutions with porosity of

632   0.5.
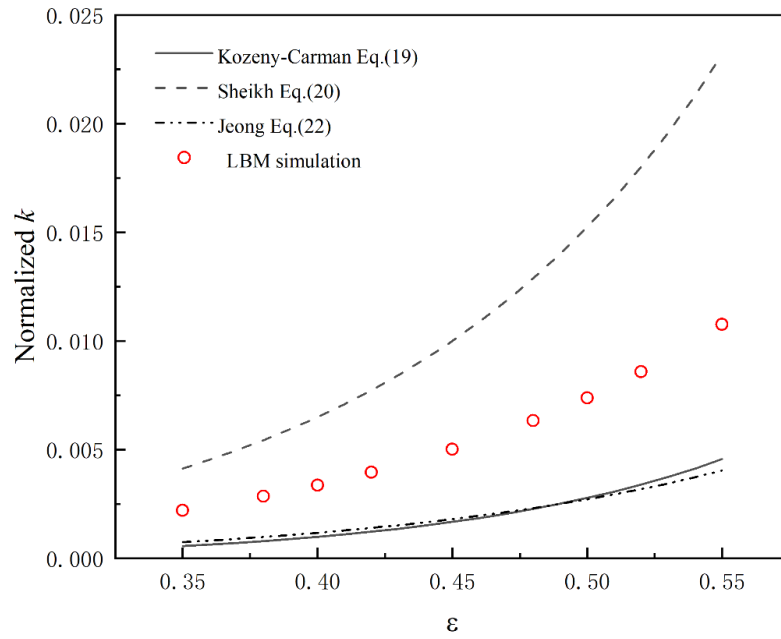
633

634   Fig. 8. Comparison between simulation results and other empirical formulas
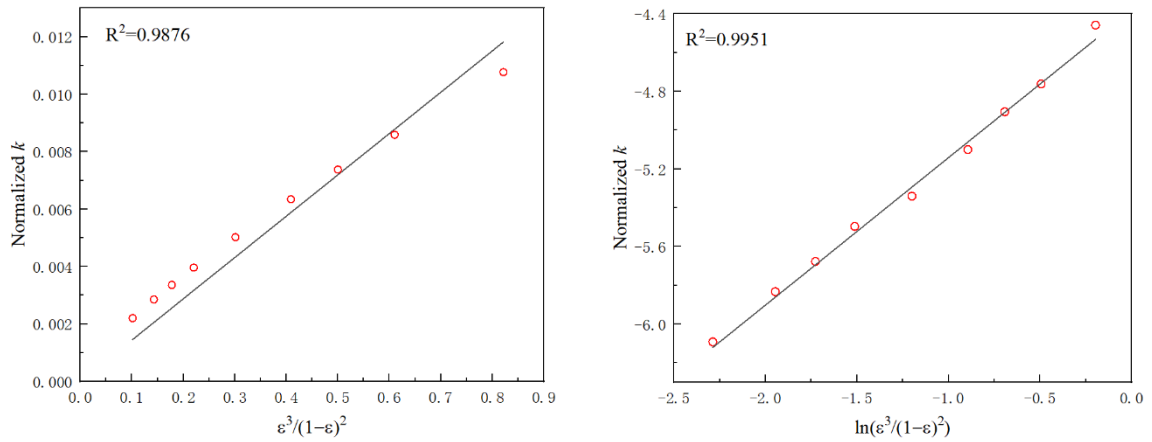
635

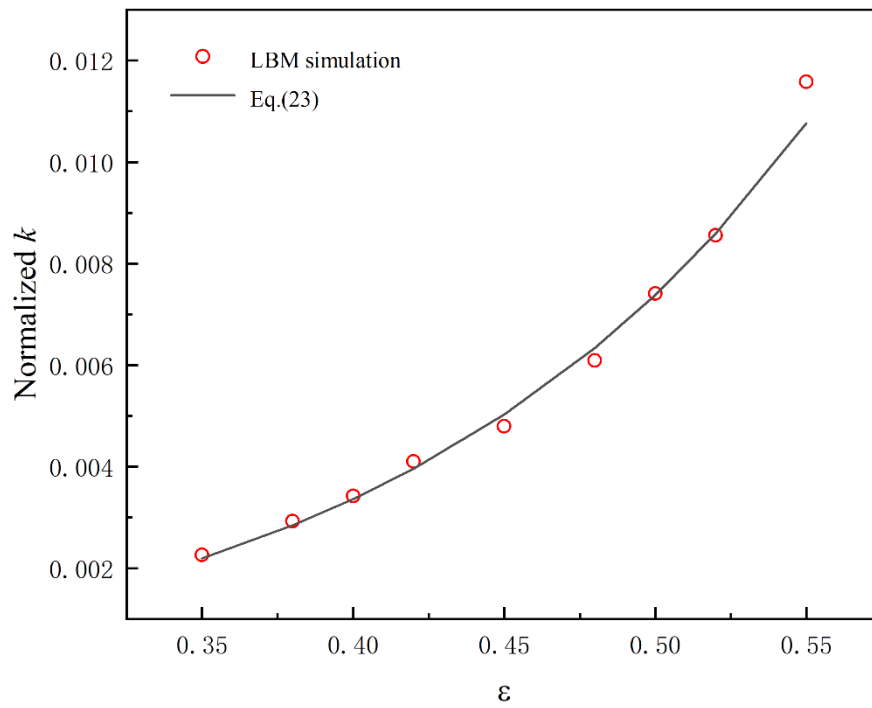636   Fig. 9. (a) Linear regression on the relative permeability K and the expression

637     $\varepsilon^3/(1-\varepsilon)^2$ of the porosity. (b) Linear regression on the relative permeability K and

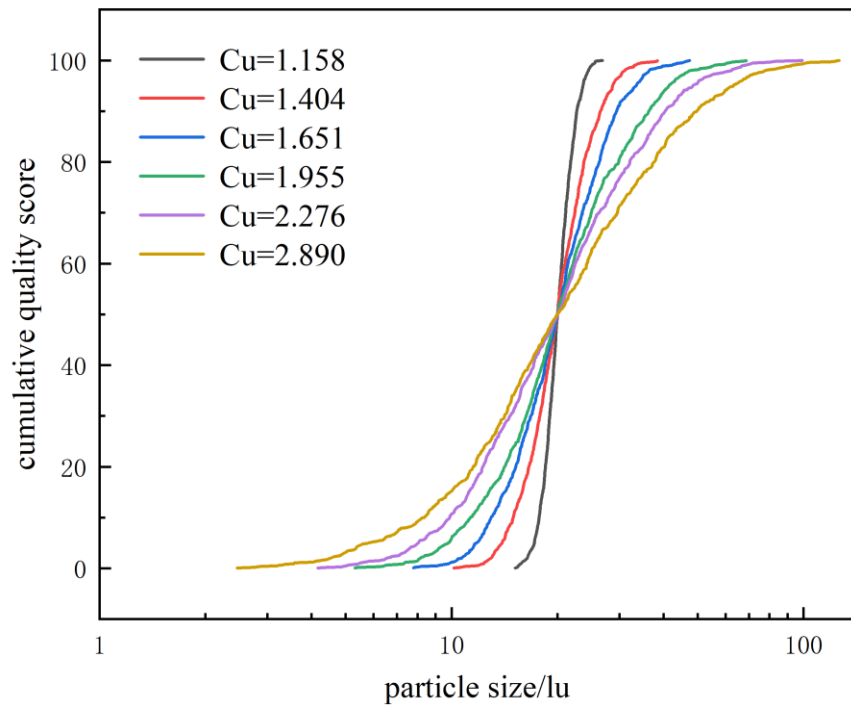638   the expression $\ln(\varepsilon^3/(1-\varepsilon)^2)$ of the porosity.
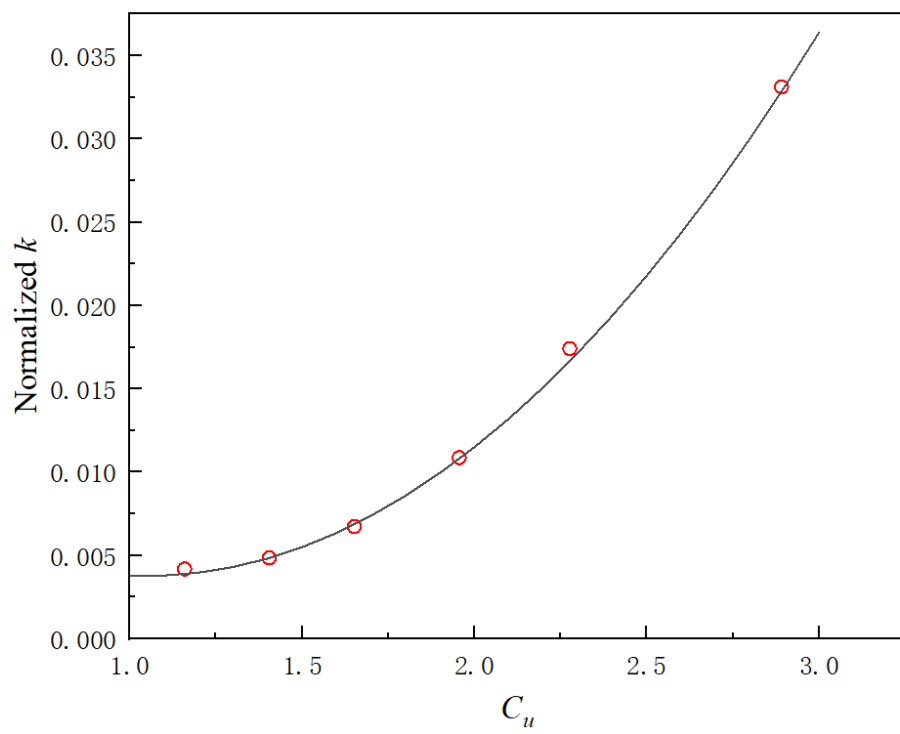
639

640

641

642

643   Fig. 10. Simulation results and the empirical formula
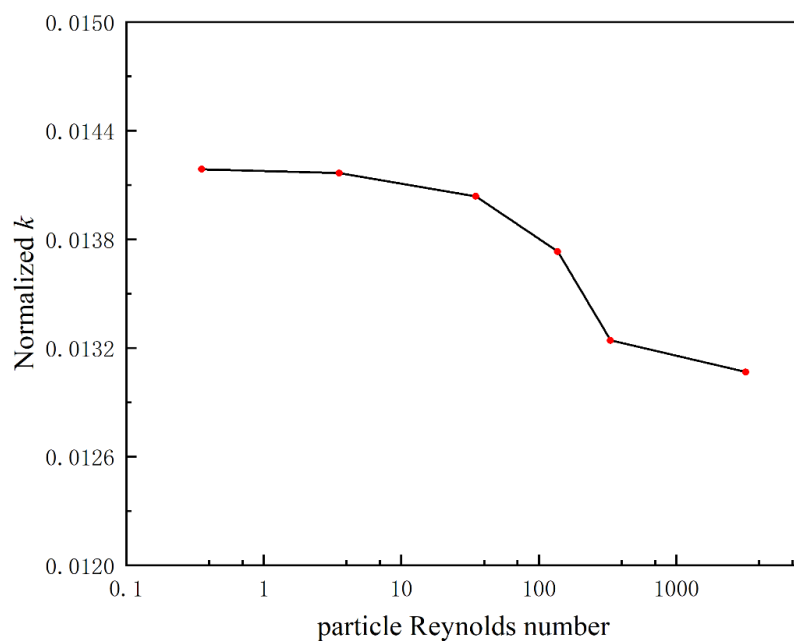
644

645

646   Fig. 11. Gradation curves for different calculation cases
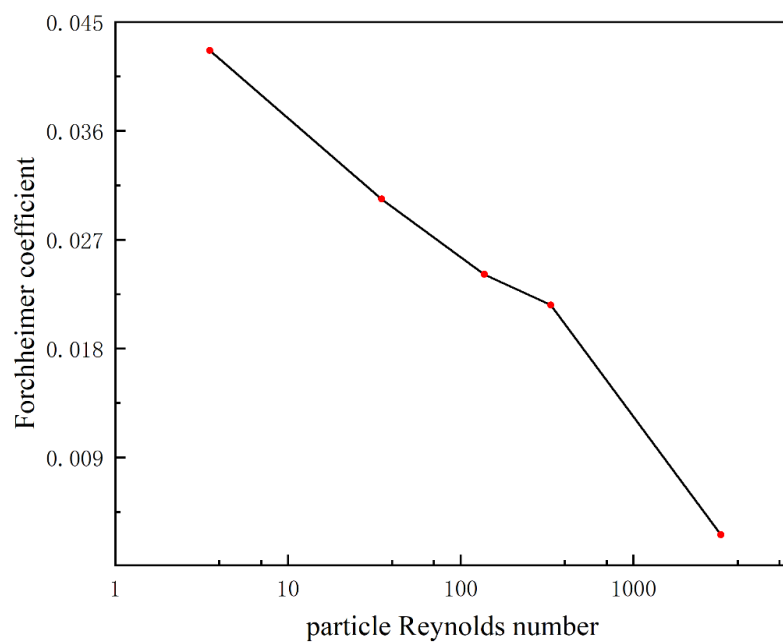

647

648   Fig. 12. Relation between the relative permeability coefficient and coefficient of

649 nonuniformity with porosity of 0.5.

650

651 Fig. 13. Permeability with different particle Reynolds numbers with porosity of 0.4.

652

653 Fig. 14 Permeability with different particle Reynolds numbers with porosity of 0.4.